

## Research Article

# A Piezoelectric-Driven Rock-Drilling Device for Extraterrestrial Subsurface Exploration

He Li <sup>1</sup>, Yi Shen <sup>2</sup>, Qingchuan Wang,<sup>2</sup> Yinchao Wang,<sup>2</sup> Deen Bai,<sup>2</sup> and Zongquan Deng<sup>2</sup>

<sup>1</sup>College of Mechanical and Electronic Engineering, Shandong University of Science and Technology, No. 579, Qianwangang Road, Huangdao District, Qingdao 266590, China

<sup>2</sup>State Key Laboratory of Robotics and System, Harbin Institute of Technology, No. 92, Xidazhi Street, Nangang District, Harbin 150001, China

Correspondence should be addressed to Yi Shen; [bhdxsy2008@163.com](mailto:bhdxsy2008@163.com)

Received 19 February 2018; Revised 4 May 2018; Accepted 27 May 2018; Published 2 July 2018

Academic Editor: Jens Twiefel

Copyright © 2018 He Li et al. This is an open access article distributed under the Creative Commons Attribution License, which permits unrestricted use, distribution, and reproduction in any medium, provided the original work is properly cited.

The rocks on extraterrestrial objects contain plenty of original geological and biological information. Drilling and sampling are an essential task in lunar exploration or future explorations of other planets like Mars. Due to the limitation of payloads, energies, and drill pressure, the investigation of a lightweight and low-powered rock-drilling device is crucial for explorations of distant celestial bodies. The ultrasonic drill driven by piezoelectric ceramics is a new drilling device that can adapt to the arduous space rock-drilling tasks in weak gravitational fields. An ultrasonic drill suitable for mounting on a planetary rover's robotic arm is developed. The ultrasonic transducer's energy conversion from electric energy to acoustic energy and the energy transmission from the horn's high-frequency vibration to the drill stem's low-frequency impact motion are analyzed to guide the design of the drill. To deeply understand the percussive drilling mechanism under high-speed impact, the interaction between the drill stem and the rock is simulated using LS-DYNA software. Drilling experiments on rocks with different hardness grades are conducted. The experiment results illustrate that the ultrasonic drill can penetrate into the hard rocks only taking a force of 6 N and a power consumption of 15 W. The study of ultrasonic drill will provide a reference method for sample collection of extraterrestrial rocks.

## 1. Introduction

The rock on extraterrestrial planets contains plenty of original geological and biological information [1]. The collection and in situ analysis of rock samples is one of the most important parts in the deep space exploration tasks [2]. In order to obtain unweathered and uncorroded rock internal samples, rotary-percussive drilling is a feasible and effective method to acquire the rock core with a certain diameter and length. The rotary-percussive devices are usually installed on the lander's work platforms and planet rover's robot arms [3, 4]. The rock exposed on the planet surface is subjected to weathering and deposition for a long time. Therefore, the drilling devices need large power consumption and axial drilling pressure to penetrate into the rocks. With regard to the future deep space exploration tasks of planets, especially the targets far from the earth, this rock collection mode of rotary-percussive drill faces severe challenges due to the

limited payloads and energies carried by probes. The power of the rotary-percussive drilling device is usually provided by electromagnet motors. The electromagnet motor will suffer the problem of temperature rise under vacuum and high temperature environment [5]. Special materials and technologies are essential to improve the motor's heat resistant performance [6]. Most seriously, the lubrication and sealing technologies of kinematic pairs become much more difficult, which will lead to the transmission components' failure [7]. When operating on the planets like Mars and asteroids with low gravity fields, the drilling devices need large axial drilling pressure to penetrate hard rocks. However, overlarge axial load may overturn the lander or the probe vehicle [8, 9]. Aimed at the deep space detection of even more distant planets, owing to the limited loading capability and power of space vehicles, the drill's design of miniaturization, lightweight, and low power consumption appears to be particularly important.

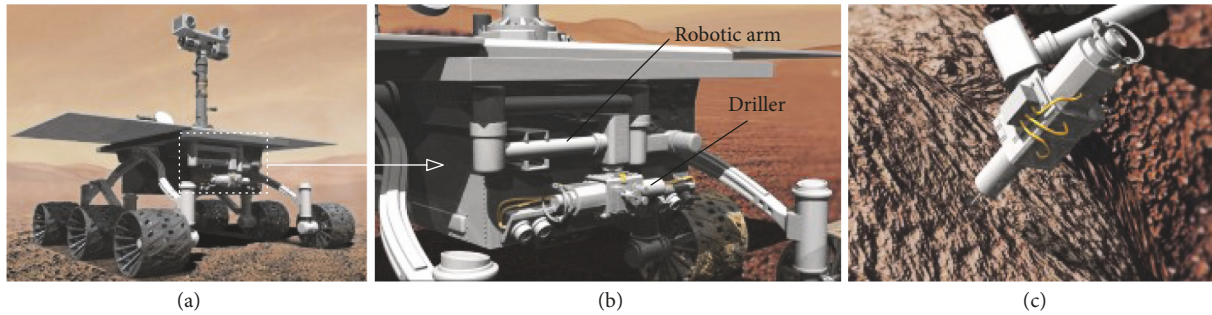


FIGURE 1: The description of rock sampling and detection mission on the extraterrestrial objects. (a) Exploration rover; (b) ultrasonic drill on the robotic arm. (c) Drilling and sampling work.

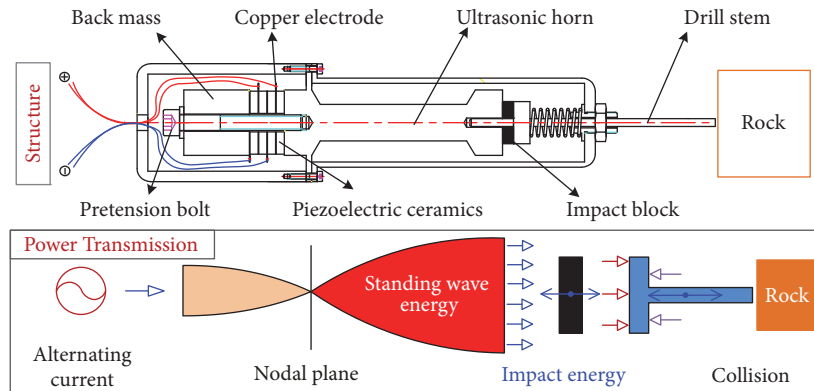


FIGURE 2: The structural composition and energy transfer process of the ultrasonic drill.

The piezoelectric-driven actuator is a kind of novel intelligent actuators which have high energy density, low power consumption, and strong environmental tolerance [10, 11]. Piezoelectric-driven actuators can realize the power conversion and transmission and have applied successfully to the fields of ultrasonic cleaning [12, 13], ultrasonic machining [14, 15], and ultrasonic motors [16, 17]. Since the piezoelectric ceramics show a wide temperature tolerance range, the ultrasonic drill actuated by piezoelectric ceramics has strong adaptive capacity in extreme environments [18].

Jet Propulsion Laboratory (JPL) is the first research institution that puts forward the concept of ultrasonic drill. This new technology shows great potential in the field of in situ sampling and analysis for planet exploration tasks. Based on ultrasonic drilling technology, JPL has successively developed ultrasonic polishing tool [19], Auto-gopher [20], rotary-assisted ultrasonic drill [21], etc. Since the birth of this technology, many international research institutes pay attention to the ultrasonic drilling or coring devices. European Space Agency (ESA) developed an ultrasonic driller/corer for the missions of “ExoMars” [22]. The influence of installation method on drilling efficiency is investigated. Biysk ultrasonic technology center and space technology institute of Russia jointly developed an ultrasonic drill tool to gather lunar soil or powdered cuttings [23]. For the sake of adapting to planetary exploration missions, University of Paderborn and University of Connecticut have also developed ultrasonic

drillers for dynamic contact analysis and studies on driving characteristics [24, 25].

For the future in situ detection of rocks on extraterrestrial objects like mars and asteroids, Research Center of Aerospace Mechanism and Control of Harbin Institute of Technology developed an ultrasonic driller/corer which is installed on the end effector of robotic arm. The driving characteristics and energy transfer process of the drill are studied, and the drilling experiments are conducted to validate the ultrasonic drill’s working performance.

## 2. Ultrasonic Drill’s Working Principle

In China’s future planetary exploration missions, rock sampling is a critical step. Figure 1 shows a conception that an ultrasonic drill installed on a planetary rover was carrying out the rock sampling task. Figures 1(a) and 1(b) show an imaginary rover and the robotic arm with an ultrasonic drill installed on the rover. When the rover marches on the planet, the robotic arm is locked. Once the on-board camera finds the sampling target, the robotic arm is unlocked, and the arm handles the drill to accomplish the rock sampling task.

The structure and working principle of the proposed ultrasonic drill are shown in Figure 2. The drill consists of back mass, piezoelectric ceramic stack, ultrasonic horn, pretension bolt, copper electrode, impact block, drill stem, etc.

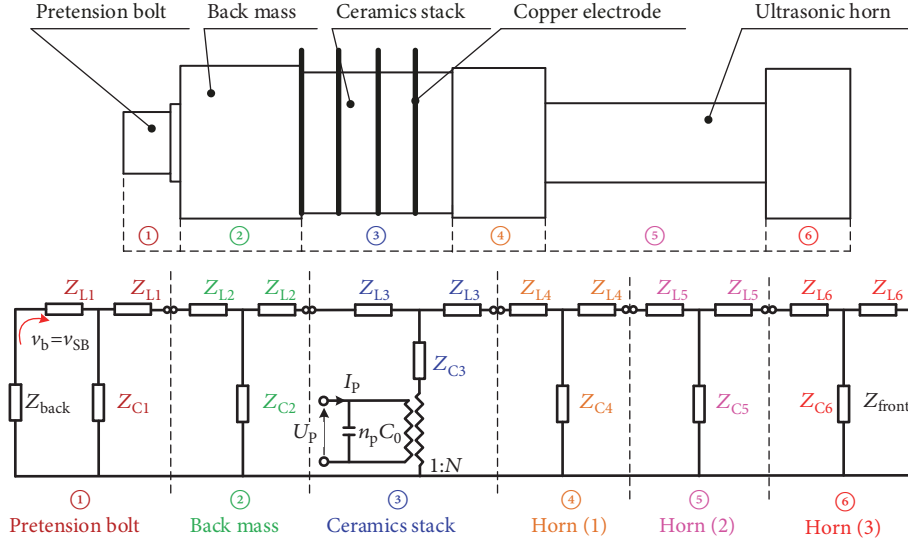


FIGURE 3: Acoustic impedance model of the ultrasonic drill's transducer.

When the piezoelectric ceramic stack is excited by high-frequency alternating current, the piezoelectric transducer will transform the high-frequency electrical signal into the high-frequency mechanical vibration due to the inverse piezoelectric effect. The ultrasonic horn's function is energy concentration; in other words, the role of the horn is to magnify the amplitude of elastic waves in the piezoelectric transducer. The vibration amplitude at the end of the horn is the maximal in the transducer. The horn, the impact block, and the drill stem form a vibration-impact system. The impact block plays a role of energy transfer unit which transform the ultrasonic frequency mechanical vibration (above 16 kilohertz) at the end of the horn into the low-frequency vibration (about several hundreds of hertz) of the drill stem. The impact of the drill stem fractures rock when its failure strain is exceeded at the interface between rock and drill stem. The emphasis of this article focuses on the analysis of the energy conversion of the standing wave energy in ultrasonic transducer, the energy transformation of the impact energy of the impact block, and the interaction between the drill stem and the rock.

### 3. Acoustic Impedance Model of the Ultrasonic Drill's Transducer

The piezoelectric transducer is the power source of the ultrasonic drill. The transducer converts the high-frequency alternating current into mechanical vibration in elastic solid. Impedance characteristics of the piezoelectric transducer reflect the magnitude of the radiated sound power. In order to acquire large impact energy toward the impact block, the transducer should operate at the resonant frequency and it is necessary to calculate the minimum impedance under resonant frequency. The method of electroacoustic analogy is adopted in the article. As shown in Figure 3, the transducer is divided into six parts: the pretension bolt, back mass, ceramics stack, and the ultrasonic horn's three sections. Each

part's impedance can be equivalent by a T-type circuit. If the impedance of the six parts is connected in series, the lumped acoustic impedance network is obtained, which is shown in Figure 3. It should be noted that the impedance of copper electrode is neglected due to its minimum impedance compared with that of the other parts. To minimize the copper electrode's impedance, the thickness of the electrode is designed as 0.2 mm. With regard to the structural design of the horn, conic section transition is adopted for vibration's smooth and steady transmission. However, the physical model of the horn's impedance is simplified as dumbbell-shaped model to facilitate computation.

In the acoustic impedance model,  $U_p$ ,  $I_p$ ,  $n_p$ , and  $C_0$  are the voltage flowing through the ceramics, the current flowing through the ceramics, the quantity of the ceramics in the stack, and the static cut-off capacitance of one piece of ceramic, respectively. The back and the front load impedances are expressed as  $Z_{back}$  and  $Z_{front}$ , respectively. Under no load condition,  $Z_{back} = Z_{front} = 0$ . The horizontal acoustic impedance  $Z_{L_i}$  and vertical acoustic impedance  $Z_{C_i}$  can be expressed as

$$Z_{L_i} = j(\rho_i c_i S_i) \tan\left(\frac{k_i l_i}{2}\right) \quad (1)$$

$$Z_{C_i} = \frac{(\rho_i c_i S_i)}{[j \sin(k_i l_i)]}$$

where  $\rho_i$ ,  $c_i$ ,  $S_i$ ,  $k_i$ , and  $l_i$  represent the average density, average sound velocity, sectional area, average wave number, and characteristic length of the  $i$ th part.

The black dotted line in Figure 4 shows the computational result of the above acoustic impedance model. The curve reveals that the ultrasonic transducer's resonant frequency is 16140 Hz, and the minimum modulus of impedance is 23  $\Omega$ . In engineering application, the frequencies over 16 kHz belong to ultrasonic frequency scope. With regard to the design of the ultrasonic drill, on the one hand, the drill is

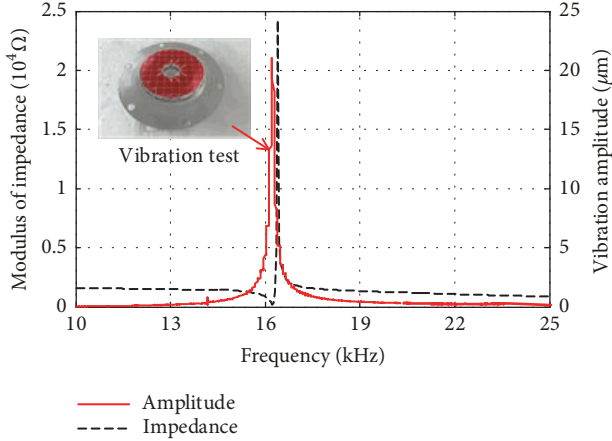


FIGURE 4: The theoretical result of the transducer's impedance model and the measuring result of the vibrating amplitude at the horn's front end.

expected to working in the range of ultrasonic frequency. On the other hand, the modulus of impedance at resonant frequency is designed as small as possible for the purpose of reducing the loss of active power and improving the acoustic power radiation efficiency. Therefore, the establishment of the impedance model can be used to guide the design of the piezoelectric transducer.

For the sake of validating the working frequency of the ultrasonic drill, the Polytec Laser Doppler Vibrometer PSV-400 is adopted to test the transducer's resonant frequency. The testing experiment result shown by the red solid line in Figure 4 demonstrates the actual operating frequency is 16148 Hz that is very close to the theoretical result. The vibration test also reveals that the output vibration amplitude of the piezoelectric transducer is about 22  $\mu\text{m}$ , which is a key parameter for the following research on the impact block's nonlinear dynamics.

#### 4. The Transmission of Impact Energy

The vibration generated by the transducer is a kind of vibration with high frequency and low amplitude. In order to penetrate into the hard rock, it is better for the drill stem to get a vibration with high amplitude and acoustic frequency. The impact block plays a role of transmission of vibration power in ultrasonic drill. The impact block obtains momentum from the bottom surface of the ultrasonic horn and then collides with the top surface of drill stem. After the collision, the impact mass get reverse momentum and collides with the horn. This process is a cyclic process. Due to the impact mass's repeated collisions with the drill stem, the drill stem will generate vibration. As a result, impact mass converts the output high-frequency mechanical vibration generated by the ultrasonic transducer into the drill stem's acoustic frequency impact action to the rock. The study of nonlinear dynamic behavior of the impact block contributes to the understanding of the energy transmission process from ultrasonic horn to the drill stem.

For the vibration-impact system, the system state variable after collision depends on the state variable before collision and is closely related to recovery coefficient and the block's momentum when collision occurs.

**4.1. Vibration System's Fundamental Assumption.** In order to investigate the kinetic characteristics of the impact block, a discrete mathematical model is established. The motion of the impact block is multiple periodic motion, and the motion will transform into chaotic motion as the change of the system motion parameters and external conditions. The excitation from the horn, the spring force on the drill stem, and the gravity of the block are the dominant factors affecting the impact block's motion. Before building the model, some reasonable assumptions are proposed which are listed as follows.

- (1) Since the piezoelectric transducer is mechanically clamped at nodal position, the collision of the impact block does not affect the vibration of the horn's front end surface, which can be expressed as simple harmonic motion, and the equilibrium position is fixed.
- (2) The motion of impact block is considered as translational motion in the vertical direction. The lateral displacement and eccentric rotation are neglected.
- (3) In the drill's working process, the displacement of the drill stem is small. Thus, the spring deformation is considered as invariable; in other words, the spring force is constant.
- (4) The energy dissipation during the collision between the horn and the impact block and the collision between the impact block and the drill stem is taken into account by introducing Newtonian recovery coefficients in the model.

**4.2. Discrete Mathematical Model Representing Impact Block's Motion.** A sketch of the vibration-impact system is shown in Figure 5. The motion of the horn's end surface is expressed as

$$u(t) = u_0 \cos(2\pi ft) \quad (2)$$

where  $f$  and  $u_0$  are the transducer's resonant frequency and output vibration amplitude, respectively. In the process of movement,  $u(t)$ ,  $y(t)$ , and  $x(t)$  satisfy the nonintrusive condition:

$$x(t) < y(t) < u(t) \quad \forall t \quad (3)$$

The state of collision system above can be represented by the state variable  $\mathbf{X}(t_j)$ . The expression of  $\mathbf{X}(t_j)$  is shown in

$$\mathbf{X}(t_j) = [t_j, x(t_j), \dot{x}(t_j^+), \dot{y}(t_j^+)]^T \quad (4)$$

where  $t_j$  is the moment when the  $j$ th collision occurs between the impact block and the drill stem;  $x(t_j)$  is displacement of the drill stem's top surface at time  $t_j$ ;  $\dot{x}(t_j^+)$  is the instantaneous velocity of the drill stem's top surface after time  $t_j$ ;  $\dot{y}(t_j^+)$  is the instantaneous velocity of the impact block after time  $t_j$ . For

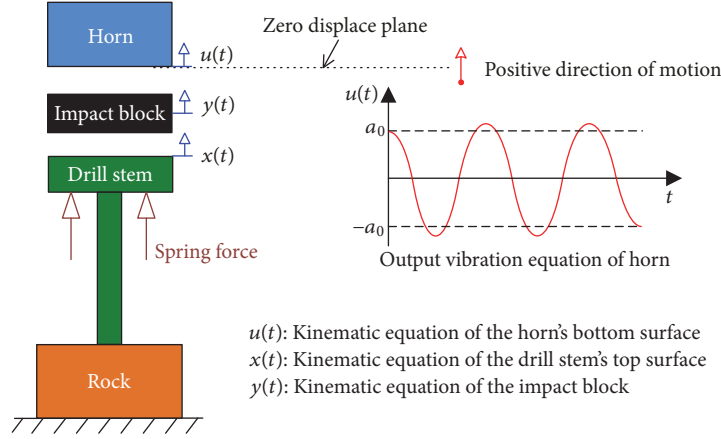


FIGURE 5: Sketch of the vibration-impact system.

the sake of simplification, corner marks listed as follows are adopted.

$$\begin{aligned}
 u_j &= u(t_j), \\
 x_j &= x(t_j); \\
 \dot{x}_j^+ &= \dot{x}(t_j^+); \\
 \dot{y}_j^+ &= \dot{y}(t_j^+); \\
 \dot{y}_k^+ &= \dot{y}(t_k^+); \\
 \dot{y}_{k+1}^+ &= \dot{y}(t_{k+1}^+)
 \end{aligned} \tag{5}$$

Thus, the system state variable is simplified as

$$X_j = [t_j, x_j, \dot{x}_j^+, \dot{y}_j^+]^T \tag{6}$$

Discrete mathematical model representing impact block's motion can be presented by a set of difference equations which can map the system variable at time  $t_j$  to the system variable at time  $t_{j+1}$ . This set of difference equations can be expressed as

$$f(X_j, X_{j+1}) = 0 \tag{7}$$

The initial system state variable is defined as  $X_0 = [t_0, x_0, \dot{x}_0^+, \dot{y}_0^+]^T$ . Between the  $j$ th collision and the  $(j+1)$ th collision of the impact block and the drill stem, the impact block may collide with the horn for one or two times. Therefore, the calculating flowchart of the impact model is shown in Figure 6. The collision times  $m$  is determined according to the actual requirement.

Firstly, the collision time  $t_k$  between impact block and horn after time  $t_j$  should be calculated. The impact block and

drill stem's equations of motion after the  $j$ th collision between the impact block and the drill stem are

$$\begin{aligned}
 x(t) &= \frac{-g + F/M}{2} (t - t_j)^2 + \dot{x}_j^+ (t - t_j) + x_j \\
 y(t) &= -\frac{g}{2} (t - t_j)^2 + \dot{y}_j^+ (t - t_j) + x_j
 \end{aligned} \tag{8}$$

$$\forall t \in [t_j, t_{j+1})$$

When the impact block collides with the horn, that is,  $y(t_k) = u(t_k)$ , then, the collision time  $t_k$  can be solved by

$$-\frac{g}{2} (t_k - t_j)^2 + \dot{y}_j^+ (t_k - t_j) + x_j = u_0 \cos(2\pi f t_k) \tag{9}$$

The second step is to calculate the next collision time  $t_{j+1}$  of impact block and drill stem. The two situations that will occur are listed as follows:

(a) The impact block collides with the horn for one time between the  $j$ th collision and the  $(j+1)$ th collision of the impact block and the drill stem. The collision time of impact block and horn  $t_k \in (t_j, t_{j+1})$ .

(b) The impact block collides with the horn for two times between the  $j$ th collision and the  $(j+1)$ th collision of the impact block and the drill stem. The collision times of impact block and horn are defined as  $t_k$  and  $t_{k+1}$ , and  $t_j < t_k < t_{k+1} < t_{j+1}$ .

If the situation (a) happens, the  $t_{j+1}$  can be figured out by

$$\begin{aligned}
 &-\frac{g}{2} (t_{j+1} - t_k)^2 \\
 &+ \{\dot{u}(t_k) - \alpha_1 [\dot{y}_j^+ - g(t_k - t_j) - \dot{u}(t_k)]\} (t_{j+1} - t_k) \\
 &+ u(t_k) \\
 &= \frac{-g + F/M}{2} (t_{j+1} - t_j)^2 + \dot{x}_j^+ (t_{j+1} - t_j) + x_j
 \end{aligned} \tag{10}$$

where  $M$ ,  $F$ ,  $g$ , and  $\alpha_1$  are the mass of the drill stem, axial force on the drill stem, gravitational acceleration, and the

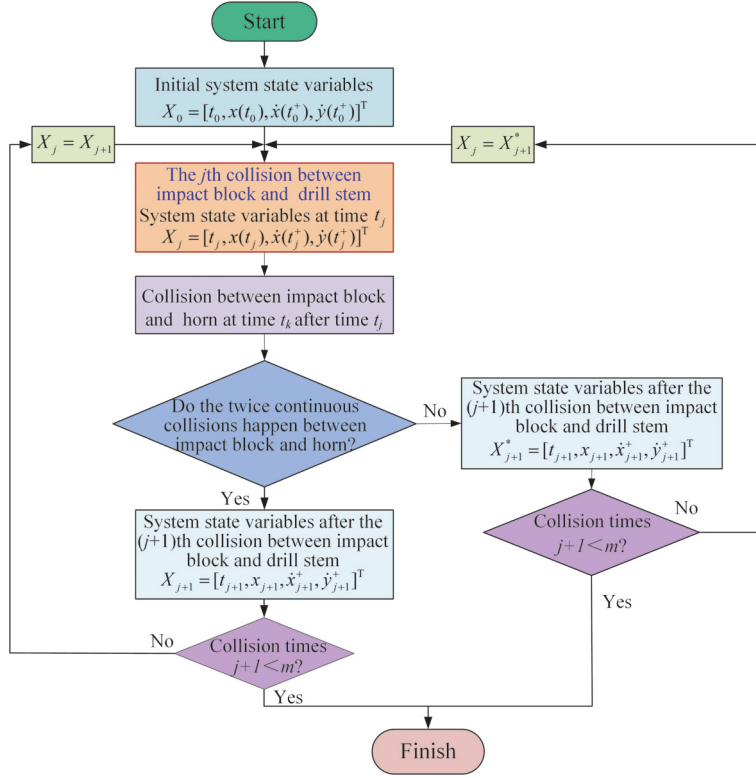


FIGURE 6: The flowchart of the impact model.

Newtonian recovery coefficient presenting the dissipation of energy during the collision between the impact block and the horn. The expression of  $\alpha_1$  is shown in

$$\alpha_1 = -\frac{\dot{y}(t_k^+) - \dot{u}(t_k)}{\dot{y}(t_k^-) - \dot{u}(t_k)} \quad (11)$$

If the situation (b) happens, the  $t_{k+1}$  should be calculated firstly by

$$\begin{aligned} & -\frac{g}{2}(t_{k+1} - t_k)^2 \\ & + \{\dot{u}(t_k) - \alpha_1 [\dot{y}_j^+ - g(t_k - t_j) - \dot{u}(t_k)]\} (t_{k+1} - t_k) \\ & + u(t_k) = u(t_{k+1}) \end{aligned} \quad (12)$$

Then, the expression of collision time  $t_{j+1}$  can be derived by the following equation.

$$\begin{aligned} & -\frac{g}{2}(t_{j+1} - t_{k+1})^2 \\ & + \{\dot{u}(t_{k+1}) - \alpha_1 [\dot{y}_k^+ - g(t_{k+1} - t_k) - \dot{u}(t_{k+1})]\} \\ & \cdot (t_{j+1} - t_{k+1}) + u(t_{k+1}) = \frac{-g + F/M}{2}(t_{j+1} - t_j)^2 \\ & + \dot{x}_j^+(t_{j+1} - t_j) + x_j \end{aligned} \quad (13)$$

For situation (a), the remaining state variables can be deduced by the following difference equations.

$$\begin{aligned} x_{j+1} &= x(t_{j+1}) \\ &= \frac{-g + F/M}{2}(t_{j+1} - t_j)^2 + \dot{x}_j^+(t_{j+1} - t_j) + x_j \\ \dot{x}_{j+1}^+ &= \dot{x}(t_{j+1}^+) \\ &= \frac{1}{1 + \mu} [(1 + \alpha_2) \dot{y}_k(t_{j+1}) + (\mu - \alpha_2) \dot{x}(t_{j+1})] \\ \dot{y}_{j+1}^+ &= \dot{y}_k(t_{j+1}^+) \\ &= \frac{1}{1 + \mu} [(1 - \mu\alpha_2) \dot{y}_k(t_{j+1}) + \mu(1 + \alpha_2) \dot{x}(t_{j+1})] \end{aligned} \quad (14)$$

where  $\mu$  and  $\alpha_2$  are quality ratio between the drill stem and the impact block and the Newtonian recovery coefficient presenting the energy dissipation during the collision between the impact block and the drill stem, respectively. The expression of  $\alpha_2$  is shown in

$$\alpha_2 = -\frac{\dot{y}_k(t_{j+1}^+) - \dot{x}(t_{j+1}^+)}{\dot{y}_k(t_{j+1}) - \dot{x}(t_{j+1})} \quad (15)$$

TABLE 1: Impact system parameters.

Parameter	$u_0$	$f$	$\mu$	$\alpha_1$	$\alpha_2$	$g$	$F/M$
Value	22 $\mu\text{m}$	16147 Hz	5	0.7	0.9	9.8 $\text{kg/m}^3$	10

TABLE 2: Initial system state variables.

Variable	$t_0$	$x_0$	$\dot{x}_0^+$	$\dot{y}_0^+$
Value	0 s	-0.01 m	0.1 m/s	0.4 m/s

For situation (b), the remaining state variables can be deduced by difference equation set (16).

$$\begin{aligned}
x_{j+1} &= x(t_{j+1}) \\
&= \frac{-g + F/M}{2} (t_{j+1} - t_j)^2 + \dot{x}_j^+ (t_{j+1} - t_j) + x_j \\
\dot{x}_{j+1}^+ &= \dot{x}(t_{j+1}^+) \\
&= \frac{1}{1 + \mu} [(1 + \alpha_2) \dot{y}_{k+1}(t_{j+1}) + (\mu - \alpha_2) \dot{x}(t_{j+1})] \\
\dot{y}_{j+1}^+ &= \dot{y}_{k+1}(t_{j+1}^+) \\
&= \frac{1}{1 + \mu} [(1 - \mu\alpha_2) \dot{y}_{k+1}(t_{j+1}) + \mu(1 + \alpha_2) \dot{x}(t_{j+1})]
\end{aligned} \tag{16}$$

**4.3. Solution and Result of the Discrete Mathematical Model.** The solution of the discrete mathematical model is a process of repetitively judging the collision situation and continuously iterating the system state variable. To acquire the movement characteristics of the impact block and the drill stem, the system parameters and initial system state variables should be provided which are shown in Tables 1 and 2. In Table 1, the values of  $u_0$  and  $f$  have been measured and calculated in Section 3, and  $\alpha_1$  and  $\alpha_2$  are calculated by (11) and (15).

The initial system state variable  $X(t_0) = [t_0, x_0, \dot{x}_0^+, \dot{y}_0^+]^T$  can be obtained by observing the impact block's motion using a high-speed camera. A set of measured data is chosen which is shown in Table 2.

The solution result is shown in Figure 7. It is obvious that motion of the impact block presents complicated nonlinear feature. This nonlinearity is mainly derived from the dissipation of energy during the collisions and different collision situation between the horn and the impact block. The impact block's displacement curve demonstrates that there is a reciprocal relationship between the distance from the horn's bottom to the drill stem's top and the vibration frequency of the impact block. That is, when the distance from the horn's bottom to the drill stem's top becomes short, the vibration frequency of the impact block becomes high, and the impact number of times becomes more, which will impel the drill stem to move downward.

Overall, the vibration-impact system including the horn, impact block, and the drill stem successfully converts the high-frequency small-amplitude vibration into the low-frequency large-amplitude vibration.

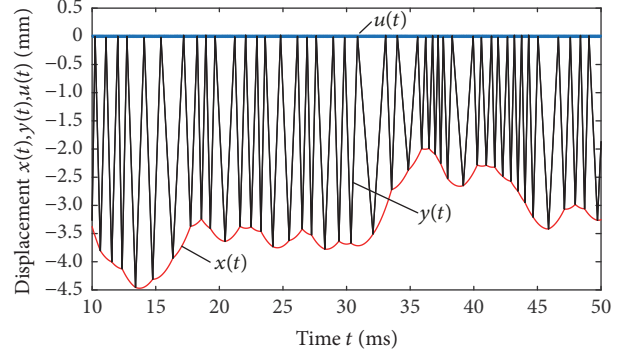


FIGURE 7: The motion of the impact block and drill stem.

## 5. Interaction between the Drill Stem and the Rock

The drilling pressure on the rock comes from the impact of the drill stem. Under high-speed impact action, the rock gradually gets broken. The study on the interaction process between rock and the drill stem contributes to deeply understanding the rock fragmentation mechanism of ultrasonic drill. Cylindrical drill stem is adopted in this section to investigate the stress distribution in the rock. As shown in Figure 8(a), when the circular section in the elastic semi-infinite space is subjected to normal distributed load, perpendicular displacement on the surface of the elastic semi-infinite space will occur. The distributed load can be expressed as

$$p = p_0 \left(1 - \frac{R^2}{a^2}\right)^n \tag{17}$$

where  $p_0$ ,  $R$ , and  $n$  are the stress at circle center, the distance from one point in stress region to the circle center, and the stress distribution index.

According to the displacement solution on Boussinesq question, superposition principle can be adopted to calculate the vertical displacement  $u_z$  on elastomer surface.

$$u_z = \frac{(1 - \nu^2)}{E\pi} \cdot \iint \frac{p}{R} dx dy \tag{18}$$

When the value of  $n$  is  $-1/2$ , the distributed load  $p$  in (17) is the load on elastomer surface when a cylindrical punch with flat fundus acts on the elastomer. In this case, the contact force  $F$  on the contact surface is

$$F = \int_0^a 2\pi R p_0 \left(1 - \frac{R^2}{a^2}\right)^{-1/2} dR = 2\pi p_0 a^2 \tag{19}$$

Thus, the relationship between the contact force  $F$  and the vertical displacement  $u_z$  is obtained as shown in

$$u_z = \frac{(1 - \nu^2)}{E} \cdot \frac{F}{2a} \tag{20}$$

According to the theory of fracture mechanics of the brittle solid, the classical Hertz cone cracks will appear in

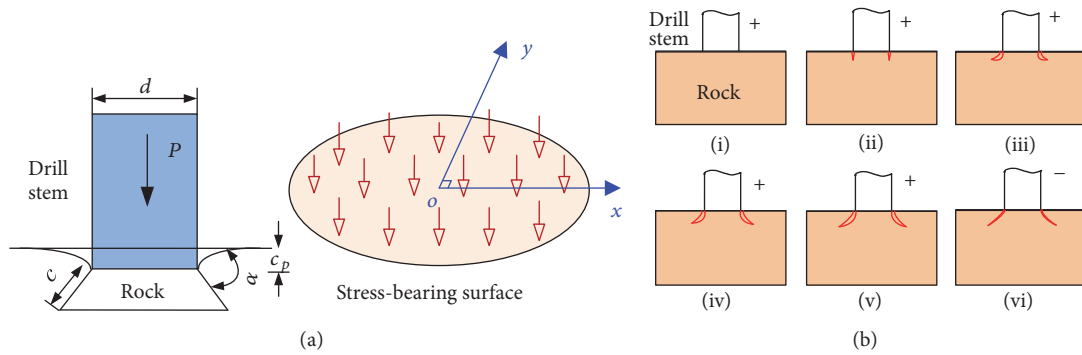


FIGURE 8: The interaction between the drill stem and the rock. (a) The load that the drill stem applies to the rock. (b) The formation and development process of Hertz cone cracks in the rock.

the rock when impacted by the cylindrical drill stem. The formation and development process of Hertz cone cracks is shown in Figure 8(b). The symbols of (+) and (-) mean the load and unload process. The loading process includes five stages, and the unloading process includes one stage. At the first loading stage, the outside region of contact zone suffers tensile stress, and then a defect begins to expand along the contact circle from an advantageous position. As a result, an annular crack is formed. After further loading, the annular crack gradually grows up in the tensile stress field. Under critical load, the developmental process of the annular crack becomes unstable, which motivates the formation of the Hertz cone-shaped body. With the increase of the load, the conical crack is in the state of stable development. When the impact load is removed as shown in Figure 8(b) (vi), the conical crack is closed. The stages from (i) to (vi) constitute a cycle period of crack development under one shock. When the rock is repeatedly impacted by the drill stem, the rock is crushed.

For the sake of obtaining the stress distribution, deformation, or invasion depth in the rock under the drill stem's impact, the explicit dynamic software LS-DYNA is adopted to simulate the interaction between the drill stem and the rock. The flowchart of the simulation process is shown in Figure 9. In the simulation model, the horn, impact block, and drill stem are defined as rigid body, and the rock is defined as elastic plastic body. The granite material is chosen for the rock. The plastic dynamics parameters of granite are shown in Table 3.

Figure 10(a) shows the entities generated in the LS-DYNA software. The contact type between the impact block and the horn or drill stem is defined as "Surface to Surface (STS)", while the contact type between the drill stem and the rock is defined as "Eroding Surface to Surface (ESTS)". In the model, a finite region is used to simulate a large piece of rock by adding nonreflecting boundary condition on the nonacting surfaces of the rock. The displacement load measured in the Section 3 is applied on the bottom surface of the horn, and the initial velocity of the impact block is set as 0.5 m/s which is chosen according to the observation using a high-speed camera. Figure 10(b) shows the stress distribution diagram

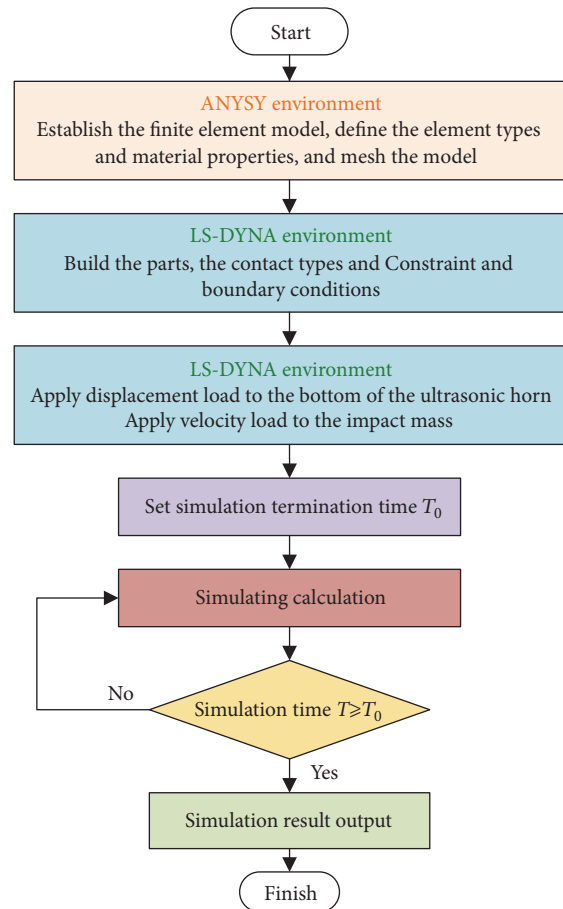


FIGURE 9: The flowchart of the simulation process using ANSYS and LS-DYNA software.

in the rock at the time of 3.8 ms when the collision occurs. In order to clearly see the deformation in the rock under the drill stem's impact, the node of No. 6114 in the contact zone is selected to calculate the invasion depth as shown in Figure 11. The result illustrates that the three collisions happen in 4 ms, and the invasion depth reaches 5  $\mu\text{m}$ . The curve

TABLE 3: Plastic dynamics parameters of granite.

Parameter	Density	Elasticity modulus	Poisson ratio	Yield strength	Failure strain
Value	2600 kg/m <sup>3</sup>	0.55×10 <sup>11</sup> Pa	0.27	1.17×10 <sup>11</sup> Pa	0.06

TABLE 4: Parameters of the ultrasonic drill prototype.

Parameter	Size diameter × length	Weight	Working frequency	Input power	impact block's mass	Drill stem's diameter
Value	34 mm × 213 mm	402 g	16148 Hz	15 W	4~6 g	6 mm

TABLE 5: Drillability levels of common rocks.

Rock type	Red brick	Sandstone	Melaleuca stone	Marble	Green rock	granite
Drillability level	3	4	5	5	6-7	10-11

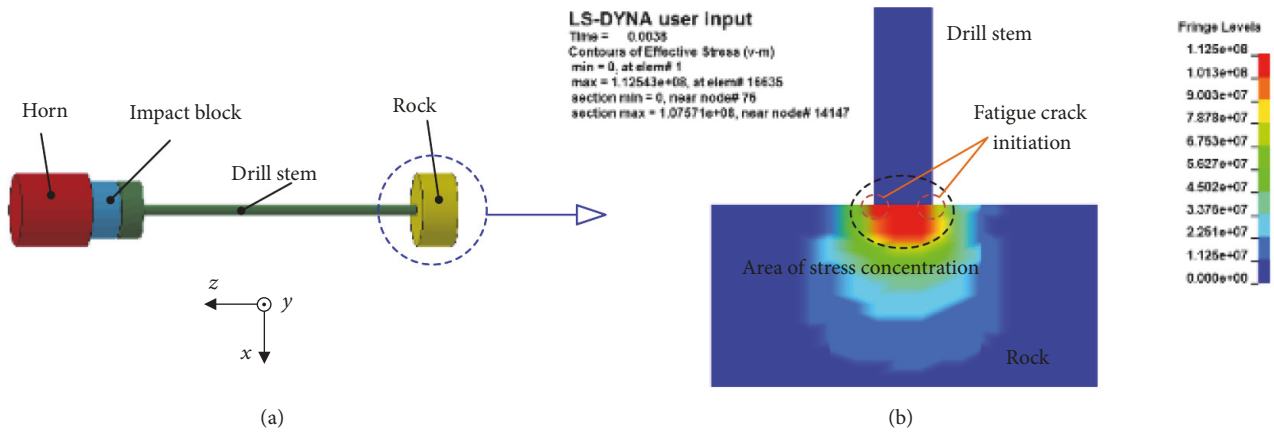


FIGURE 10: The LS-DYNA model and the simulation result. (a) LS-DYNA model. (b) Simulation result.

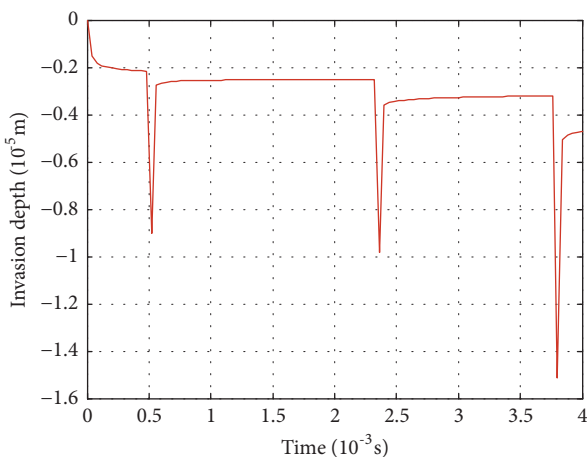


FIGURE 11: The invasion depth of the drill stem penetrating into the rock.

also reveals that the impact frequency is about from 500 to 1000 Hz, which coincides with the calculation result in Section 4. When the drill stem impacts the rock every time,

the elastic linear deformation emerges firstly in the contact area, and then the unrecoverable plastic deformation appears. Every impact from the drill stem will generate invasion with a certain depth. As a kind of hard and brittle materials, the rock will fracture when the impact force exceeds its fatigue stress.

## 6. Drilling Experiments of the Ultrasonic Drill

Based on the above theoretical analysis and simulation results, an ultrasonic drill prototype is developed. Given the constraints of the planetary exploration tasks, lightweight, low power consumption, and high drilling efficiency are regarded as design goals. The prototype's parameters are shown in Table 4.

In order to evaluate the drill's drilling performance, a testing system of the ultrasonic drill is established, and the drilling experiments of rocks with different hardness and drillability grades are carried out. The drill's experiment system shown in Figure 12 includes test bed, data acquisition system, signal generator, ceramics driver, and rock samples. The drillability levels of common rocks are listed in Table 5.

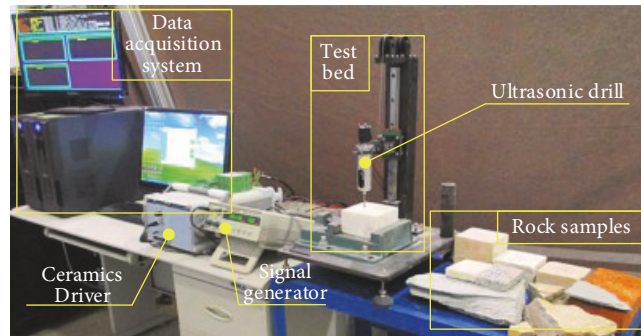


FIGURE 12: Test and experiment system of ultrasonic drill.

The drilling pressure in the experiment is set as 6 N, and the input voltage is about 138 V. A drill stem with cylinder-shaped head is adopted to drill into the different rocks chosen above. With regard to every drilling medium, the drilling experiment is repeated ten times. The mean values of the ten sets of test data are calculated, and the drilling depth curves are plotted as shown in Figure 13. In the red brick's drilling experiment, the drilling time is 10 min, and the drilling depth data are recorded every 5 min. In the sandstone's drilling experiment, the drilling time is also set as 10 min, and the drilling depth data are recorded every 1 min. For the rest four kinds of rocks, the drilling time is set as one hour, and time interval of date recording is set as 10 min due to the drilling difficulty for the drill to very hard rocks.

It is clearly seen from Figure 13 that the drilling efficiency average values of the drill for red brick, sandstone, melaleuca stone, marble, green rock, and granite are 4.5 mm/min, 3.4 mm/min, 0.42 mm/min, 0.29 mm/min, 0.28 mm/min, and 0.13 mm/min, respectively.

In the marble's drilling experiment, the power consumption of the drill is detected in real time. The power-time curve is obtained which is shown in Figure 14. The curve demonstrates that the drill's power is about 15 W during the drilling process.

The rock-drilling experiments reveal that the ultrasonic drill can penetrate into the hard rocks under small drilling pressure and low power consumption. To acquire higher drilling efficiency, improving the drill's power and optimizing the drilling pressure are the effective measures under the permission conditions of the planetary exploration tasks.

## 7. Conclusions

For future rock's in situ or sampling detection missions on distant extraterrestrial planets with weak gravitational fields, an ultrasonic drill for rock-drilling conception with the help of a robotic arm installed on a planetary rover is proposed. For ultrasonic drill, the investigation on the

energy conversion and transmission is essential. Based on the acoustic impedance model, the energy conversion process of ultrasonic drill's transducer is described by mathematical method, which contributes to the improvement of the transducer's electroacoustic transforming efficiency. A discrete mathematical model representing impact block's motion is established to reveal the vibration mode transformation from high-frequency impact to low-frequency impact. The simulation of the interaction between the drill stem and the rock in LS-DYNA software is conducted. The stress distribution in the rock is obtained and the drill's penetrating principle is understood profoundly. The rock-drilling experiments demonstrate that the ultrasonic drill can penetrate into the hard rocks under small drilling force and low power consumption. Since the drill has potentials for improvement on drilling efficiency by means of increasing the input power and optimizing the drilling pressure within allowed range, the theoretical studies on the drill's power transmission from the piezoelectric ceramics to the drill stem can guide the drill's design and optimization. The development of the ultrasonic drill will provide a feasible technological means for China's future drilling and sampling missions on comets or asteroids.

## Data Availability

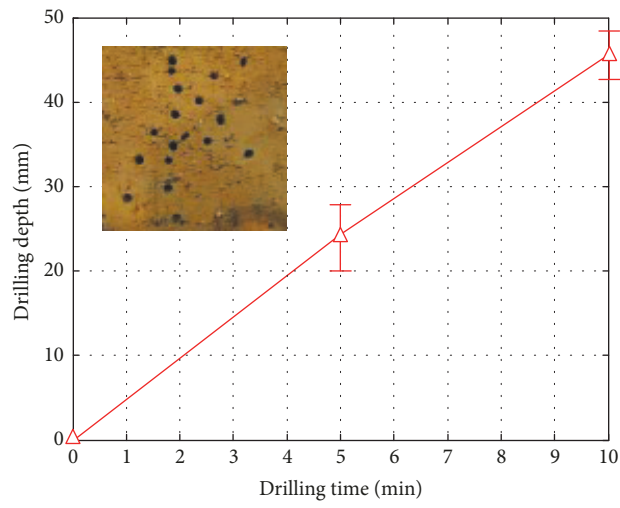
The data used to support the findings of this study are available from the corresponding author upon request.

## Conflicts of Interest

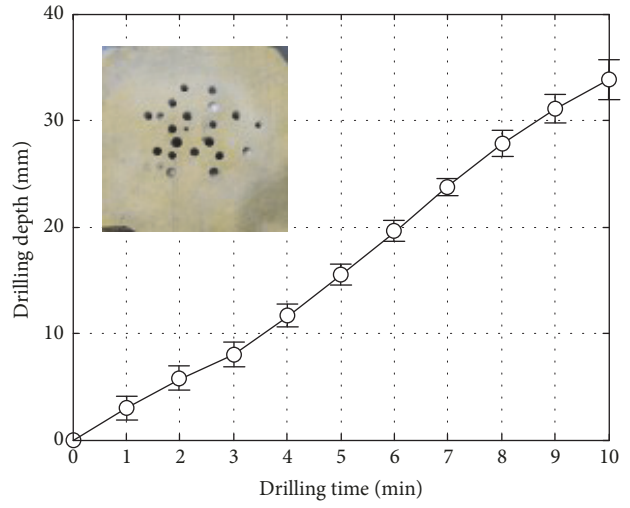
The authors declare no conflicts of interest.

## Acknowledgments

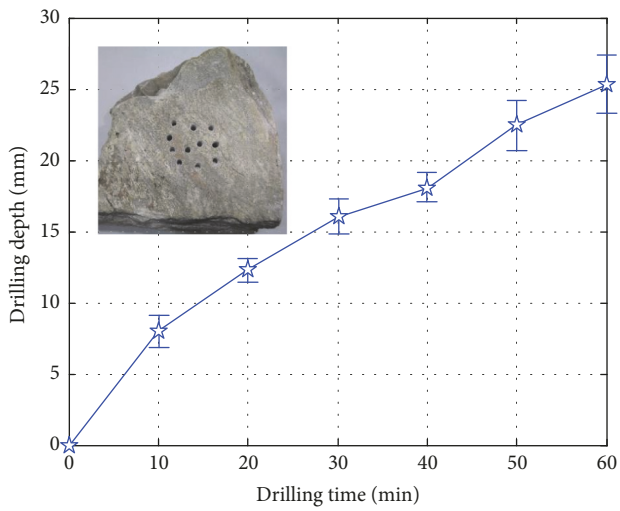
This project is supported by the Program of Introducing Talents of Discipline to Universities (B07018) and Fundamental Research Funds for the Central Universities (no. HIT.NSRIF.2014051).



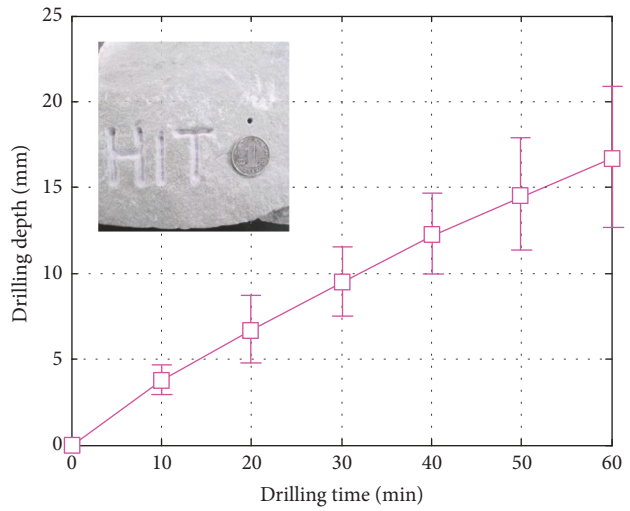
(a)



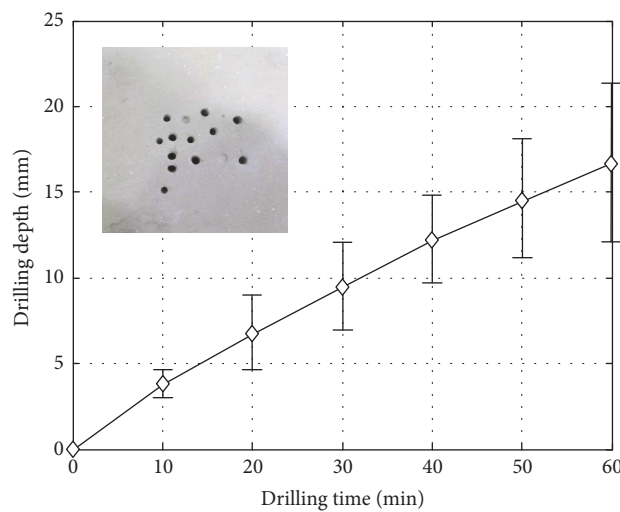
(b)



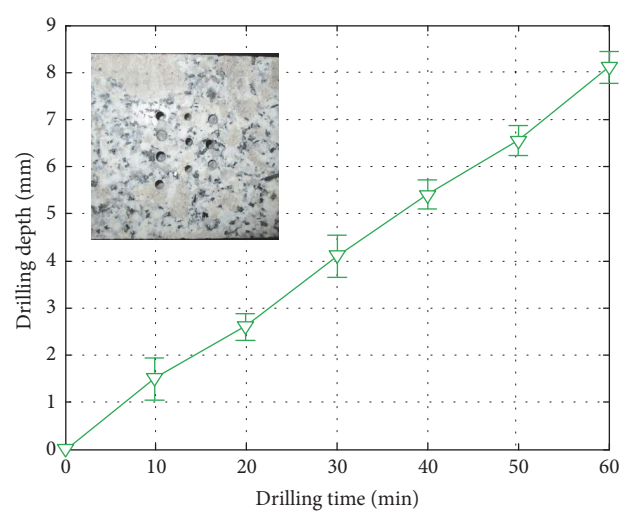
(c)



(d)



(e)



(f)

FIGURE 13: The drilling experiment results of the rocks with different hardness grades. (a) Red brick. (b) Sandstone. (c) Melaleuca stone. (d) Marble. (e) Green rock. (f) Granite.

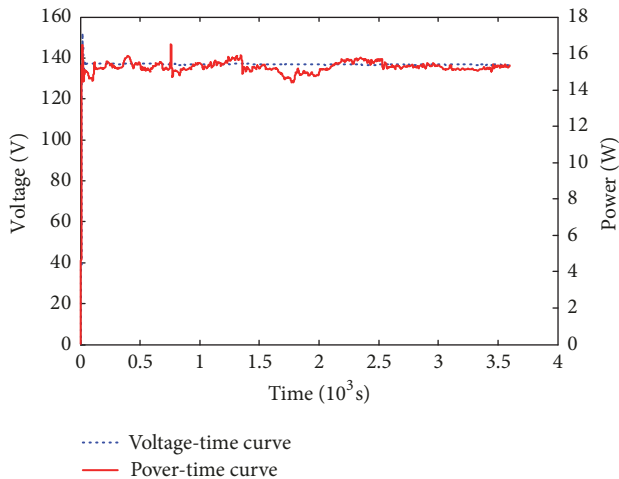


FIGURE 14: The power consumption of the drill.

## References

- [1] K. Zacny, Y. Bar-Cohen, M. Brennan et al., "Drilling systems for extraterrestrial subsurface exploration," *Astrobiology*, vol. 8, no. 3, pp. 665–706, 2008.
- [2] A. Parness, M. Frost, N. Thatte et al., "Gravity-independent rock-climbing robot and a sample acquisition tool with microspine grippers," *Journal of Field Robotics*, vol. 30, no. 6, pp. 897–915, 2013.
- [3] D. Helmick, S. McCloskey, A. Okon, J. Carsten, W. Kim, and C. Leger, "Mars science laboratory algorithms and flight software for autonomously drilling rocks," *Journal of Field Robotics*, vol. 30, no. 6, pp. 847–874, 2013.
- [4] R. C. Anderson, L. Beegle, and W. Abbey, "Drilling on mars: what we have learned from the Mars Science Laboratory Powder Acquisition Drill System (PADS)," in *In Proceedings of the 46th Lunar and Planetary Science Conference*, vol. 46, p. 2417, Woodlands, TX, USA, March 2015.
- [5] L. Weng, W. Liu, and J. Sun, "Opportunities and challenges to space tribology," *Tribology*, vol. 25, pp. 92–95, 2005.
- [6] F. F. M. El-Sousy, "Robust wavelet-neural-network sliding-mode control system for permanent magnet synchronous motor drive," *IET Electric Power Applications*, vol. 5, no. 1, pp. 113–132, 2011.
- [7] D. Morgridge, H. P. Evans, R. W. Snidle, and M. K. Yates, "A study of seal lubrication in an aerospace fuel gear pump including the effects of roughness and mixed lubrication," *Tribology Transactions*, vol. 54, no. 4, pp. 657–665, 2011.
- [8] A. E. Finzi, F. B. Zazzera, C. Dainese et al., "SD2 - How to sample a comet," *Space Science Reviews*, vol. 128, no. 1-4, pp. 281–299, 2007.
- [9] S. Tan, L. Duan, S. Tan, and H. Shi, "Study on critical drilling parameters for auger drilling," *Advanced Materials Research*, vol. 243–249, pp. 3331–3340, 2011.
- [10] F. Levassort, P. Tran-Huu-Hue, E. Ringgaard, and M. Lethiecq, "High-frequency and high-temperature electromechanical performances of new PZT-PNN piezoceramics," *Journal of the European Ceramic Society*, vol. 21, no. 10–11, pp. 1361–1365, 2001.
- [11] C. W. Law, K. Y. Tong, J. H. Li, and K. Li, "Effect of pyrolysis temperature on the characteristics of PZT films deposited by the sol-gel method," *Thin Solid Films*, vol. 335, no. 1–2, pp. 220–224, 1998.
- [12] D. D. Nguyen, H. H. Ngo, Y. S. Yoon, S. W. Chang, and H. H. Bui, "A new approach involving a multi transducer ultrasonic system for cleaning turbine engines' oil filters under practical conditions," *Ultrasonics*, vol. 71, pp. 256–263, 2016.
- [13] B. Zeqiri, M. Hodnett, and A. J. Carroll, "Studies of a novel sensor for assessing the spatial distribution of cavitation activity within ultrasonic cleaning vessels," *Ultrasonics*, vol. 44, no. 1, pp. 73–82, 2006.
- [14] Z. Y. Yu, K. P. Rajurkar, and A. Tandon, "Study of 3D micro-ultrasonic machining," *Journal of Manufacturing Science and Engineering*, vol. 126, no. 4, pp. 727–732, 2005.
- [15] D. Liu, W. L. Cong, Z. J. Pei, and Y. Tang, "A cutting force model for rotary ultrasonic machining of brittle materials," *The International Journal of Machine Tools and Manufacture*, vol. 52, no. 1, pp. 77–84, 2012.
- [16] X. Zhou, Y. Zhang, and Q. Zhang, "A novel linear ultrasonic motor with characteristic of variable mode excitation," *Ceramics International*, vol. 43, pp. S64–S69, 2017.
- [17] T. Peng, X. Wu, X. Liang, H. Shi, and F. Luo, "Investigation of a rotary ultrasonic motor using a longitudinal vibrator and spiral fin rotor," *Ultrasonics*, vol. 61, pp. 157–161, 2015.
- [18] R. Mazumder and A. Sen, "Ultra'-low-temperature sintering of PZT: A synergy of nano-powder synthesis and addition of a sintering aid," *Journal of the European Ceramic Society*, vol. 28, no. 14, pp. 2731–2737, 2008.
- [19] Z. Chang, E. H. Anderson, S. Sherrit, X. Bao, and Y. Bar-Cohen, "Design and analysis of ultrasonic horn for USDC (ultrasonic/sonic driller/corer)," in *Proceedings of the SPIE Sensors and Smart Structures Technologies for Civil, Mechanical, and Aerospace Systems*, vol. 5388, pp. 320–326, San Diego, CA, USA, 2004.
- [20] Y. Bar-Cohen, M. Badescu, S. Sherrit et al., "Deep drilling and sampling via the wireline auto-gopher driven by piezoelectric percussive actuator and EM rotary motor," in *In Proceedings of the SPIE Sensors and Smart Structures Technologies for Civil, Mechanical, and Aerospace Systems*, vol. 8345, p. 83452A, San Diego, CA, USA, March 2012.
- [21] M. Badescu, M. Tomizuka, C. Yun et al., "Percussive augments of rotary drills (PARoD)," in *Proceedings of the SPIE Sensors and Smart Structures Technologies for Civil, Mechanical, and Aerospace Systems*, vol. 8345, p. 83450J, San Diego, CA, USA, March 2012.
- [22] P. N. H. Thomas, "Magna Parva and ESA's ultrasonic drill tool for planetary surface exploration," in *Proceedings of the 12th International Conference on Engineering, Science, Construction, and Operations in Challenging Environments - Earth and Space 2010*, pp. 1235–1245, March 2010.
- [23] V. N. Khmelev, D. V. Genne, S. S. Khmelev, R. V. Barsukov, and V. I. Kostenko, "Studies of functional possibilities of model sample of the ultrasonic apparatus for drilling of the simulator of lunar soil," in *Proceedings of the 2013 IEEE 14th International Conference of Young Specialists on Micro/Nanotechnologies and Electron Devices, EDM 2013*, pp. 123–127, Russia, July 2013.
- [24] C. Potthast, J. Twiefel, and J. Wallaschek, "Modelling approaches for an ultrasonic percussion drill," *Journal of Sound and Vibration*, vol. 308, no. 3–5, pp. 405–417, 2007.
- [25] L. J. Vila and R. B. Malla, "Dynamic Impact Force on a Special Drilling Mechanism for Planetary Exploration," *Journal of Aerospace Engineering*, vol. 29, no. 4, 2016.



**Hindawi**

Submit your manuscripts at  
[www.hindawi.com](http://www.hindawi.com)

